THE JOURNAL OF PHYSICAL CHEMISTRY LETTERS
A JOURNAL OF THE AMERICAN CHEMICAL SOCIETY

pubs.acs.org/JPCL

Perspective

In Situ Active Site for Fe-Catalyzed Fischer–Tropsch Synthesis: Recent Progress and Future Challenges

Qian-Yu Liu, Cheng Shang,* and Zhi-Pan Liu*

Cite This: *J. Phys. Chem. Lett.* 2022, 13, 3342–3352

Read Online

ACCESS | Metrics & More | Article Recommendations

ABSTRACT: Fischer–Tropsch synthesis (FTS) that converts syngas into long-chain hydrocarbons is a key technology in the chemical industry. As one of the best catalysts for FTS, the Fe-based composite develops rich solid phases (metal, oxides, and carbides) in the catalytic reaction, which triggered the quest for the true active site in catalysis in the past century. Recent years have seen great advances in probing the active-site structure using modern experimental and theoretical tools. This Perspective serves to highlight these latest achievements, focusing on the geometrical structure and thermodynamic stability of Fe carbide bulk phases, the exposed surfaces, and their relationship to FTS activity. The current reaction mechanisms on CO activation and carbon chain growth are also discussed, in the context of theoretical models and experimental evidence. We also present the outlook regarding the current challenges in Fe-based FTS.

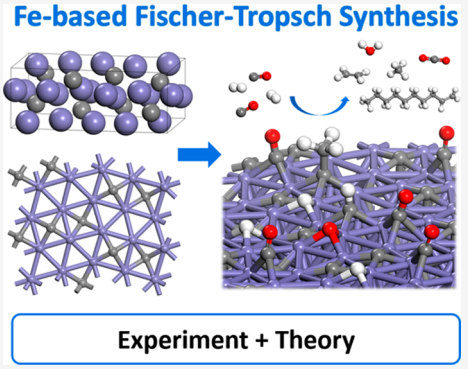

Fischer–Tropsch synthesis (FTS) is named after German chemists Franz Fischer and Hans Tropsch who succeeded in producing long-chain hydrocarbons from syngas (a mixture of CO and H_2) over Fe/ZnO or Co/Cr_2O_3 catalysts[1] in 1920s. The reaction opens the door for producing oils and chemicals from coals. After one century of extensive research, FTS has been commercialized in large quantity (400 000 barrels per day in the 2010s)[2] around the world using either Fe-based or Co-based catalysts. Fe-catalyzed FTS produces mainly long-chain α-olefins, whereas Co-based FT catalysts yield linear paraffins as primary products. Because of the abundance of Fe in the earth and the better tolerance for feedstocks with lower H_2:CO ratio (with water gas shift side reaction), Fe-based FTS catalysts have been the subject of intensive interest in the past decades.[3−8]

Industrial Fe-based catalysts are operated under high temperatures and pressures, *e.g.*, 423−623 K, 2−3 MPa, and $H_2/CO = 1-2$. The initial catalysts are generally iron oxides or/and hydroxides, which then undergo a long-time activation step (incubation) to become active catalysts. From the 1930s to the 1960s, it began to be realized that several Fe carbide (FeC_x) phases are present during FTS[9−11] in addition to metallic iron (Fe) and iron oxides (FeO_x) by *ex situ* or quasi *in situ* analysis.[12,13] The catalyst activation step is thus believed to involve the FeO_x reduction to FeC_x by CO, H_2, or syngas under the FTS conditions.[2] To date, various *in situ* formed FeC_x bulk phases, including θ-Fe_3C, χ-Fe_5C_2, Fe_7C_3, ε'-$Fe_{2.2}C$, and ε-Fe_2C have been detected according to the X-ray diffraction (XRD) and Mössbauer spectroscopy.[11,14−16] These FeC_x phases often coexist as a mixture under FTS conditions, and it is extremely difficult to distinguish their roles in FTS activity.[17,18]

As early as the 1970s, when surface science techniques became available, CO hydrogenation has been conducted on Fe metal surfaces[19−22] aiming to provide insights into FTS. Two types of carbon, "carbidic" (atomic) and "graphitic", were found to grow on the polycrystalline Fe foil, which can be distinguished by quasi *in situ* Auger electron spectroscopy (AES) and X-ray photoelectron spectroscopy (XPS).[21] The clean iron surfaces are confirmed to be thermodynamically unstable even at ultrahigh-vacuum conditions (below 1×10^{-10} mbar) after the treatment of CO and H_2 at 1 bar. In the 1990s, four types of carbon species were further distinguished from used iron FT catalysts by temperature-programmed hydrogenation:[23,24] (i) adsorbed surface atomic carbon, (ii) amorphous surface methylene chains or films, (iii) bulk iron carbide, and (iv) graphitic carbon. Type i atomic carbon was regarded to be responsible for surface polymerization because the initial catalytic activity was found to be positively correlated with the amount of atomic carbon formed on the catalyst surface.[24] The formation of a type iii iron carbide thin layer was pictured recently by using scanning tunneling microscopy (STM)[25,26] to observe the insertion of C into Fe metal interstices.

However, because of the difficulty of obtaining single-crystal FeC_x phases, the surface chemistry for FeC_x under FTS

Received: February 23, 2022
Accepted: April 1, 2022
Published: April 8, 2022

https://doi.org/10.1021/acs.jpclett.2c00549
J. Phys. Chem. Lett. 2022, 13, 3342−3352

Table 1. Signatures of FeC_x Bulk Phases Related to FTS from Different Characterization Techniques

				XRD (Cu Kα)							Mössbauer			EXAFS			
				experiment				simulation									
phase	symmetry	coordination pattern[a]	formation free energy[b] (eV/C atom, μ_C = −6.90 eV)	2θ (deg)	d (Å)	intensity	(hkl)	2θ (deg)	d (Å)	(hkl)	isomer shift (relative to α-Fe, mm/s)	hyperfine field (T)	ref	first Fe−C shell (Å)	first Fe−Fe shell (Å)	second Fe−Fe shell (Å)	ref
θ-Fe_3C	*Pnma*	TP	−0.45	42.88	2.107	57	(211)	43.37	2.084	(211)	Fe1 0.44[c]	20.8 (295 K)	52	1.94	2.52	3.73	17
#35-0772	(#62)			43.74	2.068	67	(102)	44.30	2.043	(102)	Fe2 0.44[c]	20.6 (295 K)		1.97	2.55	3.67	61
				44.57	2.031	56	(220)	45.01	2.012	(220)	Fe1 0.33	25.3 (0 K)	53				
				44.99	2.013	100	(031)	45.35	1.998	(031)	Fe2 0.33	26.6 (0 K)					
				45.86	1.977	53	(112)	49.64	1.835	(211)	Fe1 0.24	25.6 (RT)	8				
											Fe2 0.29	24.9 (RT)					
χ-Fe_5C_2	*C*2/*c*	TP	−0.51	40.85	2.207	34	(11$\bar{2}$)	41.42	2.178	(11$\bar{2}$)	Fe1 0.43[c]	18.9 (295 K)	54	1.97	2.53	3.60	17
#36-1248	(#15)			41.17	2.191	27	(202)	41.65	2.167	(202)	Fe2 0.51[c]	21.8 (295 K)		1.99	2.58		60
				43.47	2.080	66	(021)	44.01	2.056	(021)	Fe3 0.47[c]	11.0 (295 K)		1.96	2.57	3.66	61
				44.16	2.049	100	(510)	44.15	2.038	(510)	Fe1 0.39	26.1 (0 K)	53				
				45.08	2.010	35	(31$\bar{2}$)	47.80	1.901	(221)	Fe2 0.35	22.7 (0 K)					
											Fe3 0.33	13.8 (0 K)					
											Fe1 0.29	21.8 (300 K)	18				
											Fe2 0.28	18.4 (300 K)					
											Fe3 0.26	11.4 (300 K)					
o-Fe_7C_3-II	*Pnma* (#62)	TP	−0.52					39.65	2.271	(002)				1.96	2.57	3.62	61
								42.71	2.116	(240)							
								43.80	2.065	(102)							
								43.88	2.061	(071)							
								44.84	2.019	(231)							
o-Fe_7C_3	*Pnma*	TP	−0.52	39.98	2.253	54	(024)	42.86	2.108	(211)	Fe1 0.20	16.3 (300 K)	18	1.97	2.57	3.69	61
#75-1499	(#62)			39.98	2.253	54	(015)	42.92	2.106	(202)	Fe2 0.21	18.5 (300 K)					
				42.60	2.120	100	(202)	45.12	2.008	(131)	Fe3 0.25	20.5 (300 K)					
				42.60	2.120	100	(211)	45.38	1.997	(124)	Fe4 0.32	22.9 (300 K)					
				44.90	2.017	84	(115)	45.53	1.991	(115)	Fe1 0.34[d]	22.9[d]	53				

https://doi.org/10.1021/acs.jpclett.2c00549
J. Phys. Chem. Lett. 2022, 13, 3342−3352

Table 1. continued

				XRD (Cu Kα)													
				experiment				simulation			Mössbauer			EXAFS			
phase	symmetry	coordination pattern[a]	formation free energy[b] (eV/C atom, μ_C = −6.90 eV)	2θ (deg)	d (Å)	intensity	(hkl)	2θ (deg)	d (Å)	(hkl)	isomer shift (relative to α-Fe, mm/s)	hyperfine field (T)	ref	first Fe−C shell (Å)	first Fe−Fe shell (Å)	second Fe−Fe shell (Å)	ref
				44.90	2.017	84	(124)				Fe2 0.29[d]	18.7[d]					
											Fe3 0.28[d]	22.9[d]					
											Fe4 0.22[d]	19.9[d]					
											Fe5 0.22[d]	17.4[d]					
h-Fe_7C_3	$P6_3mc$	TP	−0.45	39.95	2.255	30	(210)	40.18	2.242	(210)	Fe1 0.30[d]	24.8[d]	53	1.97	2.57	3.69	61
#17-0333	(#186)			42.57	2.122	40	(102)	43.43	2.082	(102)	Fe2 0.22[d]	15.9[d]					
				44.86	2.019	100	(211)	45.25	2.002	(211)	Fe3 0.20[d]	20.0[d]					
				50.46	1.807	20	(202)	50.47	1.807	(301)							
ε′-$Fe_{2.2}C$	$P6_3/mmc$	O		37.69	2.385	25	(100)				Fe1 0.50[c]	17.3 (295 K)	54				
#36-1249	(#194)			41.48	2.175	25	(002)				Fe1 0.30[e]	25.9[e]	55				
				43.23	2.091	100	(101)				Fe2 0.30[e]	23.2[e]					
				57.28	1.607	13	(10$\bar{2}$)				Fe3 0.30[e]	18.6[e]					
				68.03	1.377	16	(110)				Fe4 0.30[e]	18.1[e]					
											Fe5 0.30[e]	17.7[e]					
											Fe6 0.20[e]	17.0[e]					
ε-Fe_2C	$P6_3/mmc$	O		37.69	2.385	25	(100)				Fe1 0.24	23.0 (RT)	56	1.91	2.73	3.90	57
#36-1249	(#194)			41.48	2.175	25	(002)				Fe2 0.22	17.4 (RT)					
				43.23	2.091	100	(101)				Fe1 0.24	14.2 (RT)	57				
				57.28	1.607	13	(10$\bar{2}$)				Fe2 0.25	17.2 (RT)					
				68.03	1.377	16	(110)				Fe3 0.17	23.5 (RT)					
											Fe1 0.20[e]	18.0[e]	55				
η-Fe_2C	$Pnnm$	O	−0.54	37.04	2.425	18	(101)	37.13	2.420	(101)	Fe1 0.28	17.8 (RT)	58	1.91	2.71	3.83	61
#37-0999	(#58)			41.81	2.159	30	(020)	42.09	2.145	(020)	Fe1 0.29[e]	17.9[e]	55				
				42.76	2.113	100	(111)	42.88	2.108	(111)							
				43.76	2.067	46	(210)	43.99	2.057	(210)							
				57.09	1.612	17	(121)	57.35	1.605	(121)							
				68.37	1.371	17	(301)										

[a]TP, triangular prism; O, octahedron. [b]Formation free energy calculated by $\Delta G_f(FeC_x) = [G(FeC_x) - G(Fe) - x\cdot\mu_C]/x$, where $G(FeC_x)$ and $G(Fe)$ are the Gibbs free energy of the FeC_x phase and Fe metal (bcc phase) [c]Isomer shift relative to the sodium nitroprusside ($Na_2[Fe(CN)_5NO]\cdot 2H_2O$, National Bureau of Standards). [d]Mössbauer parameters simulated by theoretical methods (GGA-PBEsol), 0 K. [e]Mössbauer parameters simulated by theoretical methods (GGA-PBE), 0 K.

https://doi.org/10.1021/acs.jpclett.2c00549
J. Phys. Chem. Lett. 2022, 13, 3342−3352

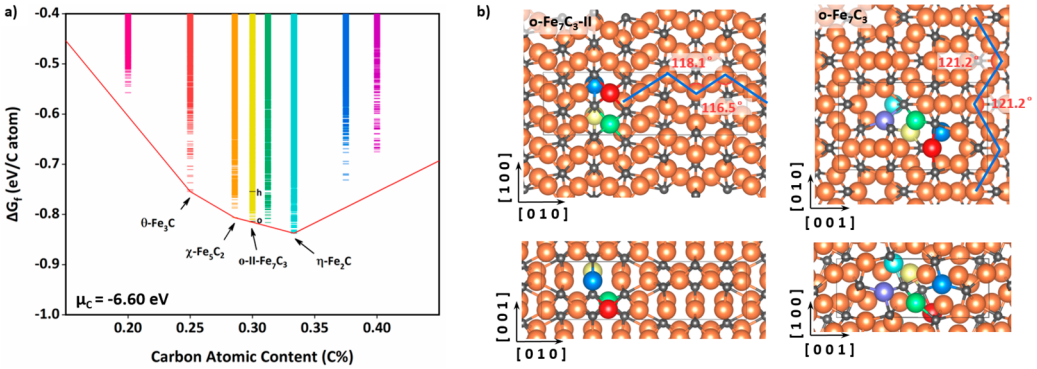

Figure 1. (a) Thermodynamic convex hull diagram for bulk FeC_x referring to Fe (bcc phase) at $\mu_C = -6.60$ eV. (b) Structures of o-Fe_7C_3-II (*Pnma*, #62, $a = 4.96$ Å, $b = 16.19$ Å, $c = 4.54$ Å) and o-Fe_7C_3 (*Pnma*, #62, $a = 4.51$ Å, $b = 6.84$ Å, $c = 11.74$ Å). Fe, orange, C, gray. Different layers of Fe atoms in o-Fe_7C_3-II and o-Fe_7C_3 are labeled with different colors (yellow, blue, green, red, cyan, and purple). Reproduced from ref 51. Copyright 2021 American Chemical Society.

conditions remains largely unknown in experiment. Since the 2000s, density functional theory (DFT) calculations have been popularly carried out for a series of surfaces of Fe metal, Fe_4C, θ-Fe_3C, χ-Fe_5C_2, Fe_7C_3, and ε-Fe_2C phases by using the bulk-truncated surface structures.[27−40] Because different surface models (e.g., surface C and H coverage) were utilized, different reaction mechanisms for CO activation and carbon chain growth have been proposed.[29−33,37−42] For CO activation, for example, at least four different mechanisms were reported: (i) direct dissociation over Fe sites; (ii) H-assisted CO dissociation on Fe sites; (iii) CH_x-assisted CO dissociation on C sites of Fe-carbide surfaces; and (iv) C-vacancy-mediated direct dissociation on Fe-carbide surfaces.

This Perspective, with a focus on the fundamental aspects of FTS, serves to highlight the latest experimental and theoretical progress on the structural features of FeC_x bulk and surfaces and their connection to FTS activity. The uncertainties regarding the *in situ* FeC_x active site and future challenges for understanding Fe-based FTS will be discussed. Readers interested in the catalyst preparation, applications, and deactivation of Fe-based FTS catalysts may refer to previous reviews.[13,43−45]

FeC_x Bulk Phases. Eight FeC_x phases at five different Fe:C ratios, namely, Fe_3C, Fe_5C_2, Fe_7C_3, $Fe_{2.2}C$, and Fe_2C, have been detected in FTS. Despite the complexity in bulk phases, the local Fe−C coordination patterns are relatively simple, with only two types. The two types are the triangular prism (TP) for θ-Fe_3C, χ-Fe_5C_2, o-Fe_7C_3-II, o-Fe_7C_3, and h-Fe_7C_3 phases and the octahedron (O) for ε'-$Fe_{2.2}C$, ε-Fe_2C, and η-Fe_2C phases. Obviously, the high C content will favor the octahedron pattern. In Table 1 we list the signatures of these FeC_x bulk phases in XRD, Mössbauer spectroscopy, and extended X-ray absorption fine structure (EXAFS), including the data from both experiments and theoretical simulations updated based on the previous review by Weckhuysen *et al.*[13]

The thermodynamic stability of the FeC_x phases is sensitive to the chemical potential of C (μ_C) that is controlled by the FTS condition (*e.g.*, temperature and pressure of CO and H_2). By conducting DFT calculations[17] on ε-Fe_3C, θ-Fe_3C, χ-Fe_5C_2, h-Fe_7C_3, ε'-$Fe_{2.2}C$, ε-Fe_2C and η-Fe_2C phases based on experimental crystal data, de Smit *et al.* showed the formation energy of various FeC_x phases is close, *i.e.*, within ~0.1 eV per C atom. They suggested that while $Fe_{2.2}C$ and Fe_2C phases are enthalpically most stable during FTS conditions, because of their higher deformation energy of the Fe sublattice ($1.6−2.0 \times 10^{-2}$ eV/C atom) with respect to Fe (bcc phase) and the higher C concentration, the kinetic factors such as strain and carbon diffusion barrier may inhibit their formation. On the other hand, χ-Fe_5C_2 has the lowest theoretical deformation energy (8.4×10^{-3} eV/C atom) and is thus more likely to form during FTS.

By using global neural network (G-NN) potential combined with stochastic surface walking (SSW) global optimization,[46−50] the global potential energy surface (PES) for FeC_x phases has been explored recently by our group, and the thermodynamic convex hull for FeC_x phases at typical FTS conditions ($-7.43 \leq \mu_C \leq -6.60$ eV) was constructed,[51] as shown in Figure 1a. We showed that three bulk phases, namely, Fe_5C_2, Fe_7C_3, and Fe_2C, are stable under FTS in producing olefins, where Fe_7C_3 and Fe_2C have rather complex PES with multiple energetically nearly degenerate bulk crystal phases. At high CO conversion, low limit of μ_C, the high Fe:C ratio FeC_x bulk phases are no longer the convex points and the catalyst becomes Fe_2C-dominated.

It is noted that the SSW global structure search[46,50] identifies a new Fe_7C_3 phase (see Table 1), *i.e.*, o-Fe_7C_3-II,[51] which is the global minimum for Fe_7C_3 composition but has the nearly degenerate formation energy with the known o-Fe_7C_3 (isostructural with Mn_7C_3). Their structures are shown in Figure 1b. The simulated XRD and EXAFS data of o-Fe_7C_3-II are also shown in Table 1 for comparison. The long-suspected Fe_7C_3 phase, h-Fe_7C_3, is thermodynamically unstable according to our formation energy data.

The XRD data (Table 1) show that the major peaks of FeC_x phases locate in the range of 42−45° (2θ) corresponding to the interplanar spacings from 2.01 to 2.12 Å. For example, for the commonly observed χ-Fe_5C_2, the major peaks are at 44.16°, 43.47°, 45.08°, 40.85°, and 41.17°, which correspond to the crystal planes (510), (021), (31$\bar{2}$), (11$\bar{2}$), and (202), respectively. The three phases with the octahedron Fe−C coordination, *i.e.*, ε'-$Fe_{2.2}C$, ε-Fe_2C, and η-Fe_2C, have very smilar XRD major peaks, manifesting the same hexagonal close packing (hcp) Fe sublattice. They differ mainly in the distrubtion of C atoms in the octahedral interstices, *i.e.*, randomly distributed in ε'-$Fe_{2.2}C$ and ε-Fe_2C, and arranged alternatively along the close-packed line in η-Fe_2C. The regular C distribution leads to the presence of the additional (210) peak at $2\theta = 43.76°$ for η-Fe_2C.

Mössbauer spectroscopy is another important technique to characterize different Fe-containing phases (Fe, FeO_x, and FeC_x). Table 1 lists the Mössbauer data from the literature.[8,18,52−58] It shows that θ-Fe_3C, χ-Fe_5C_2, and η-Fe_2C have two, three, and one set of Mössbauer parameters, respectively,

https://doi.org/10.1021/acs.jpclett.2c00549
J. Phys. Chem. Lett. 2022, 13, 3342−3352

reflecting the number of unique types of Fe atoms in different phases.

This agrees with our theoretical data of the structure fingerprint, which show two (7.27×10^{-3} and 1.07×10^{-2}), three (2.88×10^{-3}, 3.33×10^{-3}, and 5.00×10^{-3}), and one (1.57×10^{-2}) set of distance-weighted Steinhart order parameter (OP_2)[59] values for Fe atoms in θ-Fe_3C, χ-Fe_5C_2, and η-Fe_2C phases, respectively. For the other FeC_x phases, there is a lack of consistency in the Mössbauer parameters between theory and experiment. For example, o-Fe_7C_3 exhibits five sets of parameters from the simulation by Liu *et al.*,[53] but there are only four sets of parameters reported in experiment.[18] Interestingly, from our results of Fe OP_2 values, while there are indeed five different types of Fe atoms ($OP_2 = 1.71 \times 10^{-3}$, 1.79×10^{-3}, 1.87×10^{-3}, 2.81×10^{-3}, and 3.91×10^{-3}) in o-Fe_7C_3, only four different types of Fe atoms ($OP_2 = 1.26 \times 10^{-3}$, 2.28×10^{-3}, 3.28×10^{-3}, and 3.75×10^{-3}) are found in o-Fe_7C_3-II.

DFT functional has been benchmarked on the accuracy of Mössbauer parameters by Liu *et al.*,[53] which shows that the GGA-level DFT functionals, especially PBEsol, succeed in predicting Mössbauer spectra for FeC_x. The higher-level functionals, such as meta-GGA and hybrid functionals, do not necessarily provide improved results based on the comparison using the full-potential linear-augmented plane wave calculations with different functionals (LDA, GGA (PBE, PBEsol, and GGA+U), meta-GGA, and hybrid functionals).

The radial distribution function (RDF) as detected by EXAFS can be utilized to distinguish the Fe−C coordination pattern. The data from both the literature and simulation[17,57,60,61] indicate that FeC_x with the triangular prism and the octahedron coordination pattern are very different in RDF. FeC_x with the triangular prism coordination have longer Fe−C distance (1.94−1.99 Å) but shorter Fe−Fe distance (2.52−2.58 and 3.60−3.73 Å for first and second shell), compared to the octahedron coordination (1.91, 2.71−2.73, and 3.83−3.90 Å for first Fe−C, first Fe−Fe, and second Fe−Fe shell).

FeC_x Surfaces. While it is well-accepted that the FT catalyst surfaces decorated with carbidic carbons should be the active site, the atomic-level picture for the carbide surfaces under FTS conditions has long been a mystery, not only because of the pressure gap between the surface characterization techniques (<1 mbar) and FTS *operando* conditions (10−30 bar) but also because of the great structure similarity among surfaces of different FeC_x phases.

Recent years have seen encouraging progress regarding probing the surface nature of the as-synthesized FeC_x catalyst by using transmission electron microscopy (TEM), XPS, and Raman spectroscopy. According to high-resolution TEM,[18,60,62−64] the FT catalyst has a complex core−shell structure with a carbide core and an amorphous carbon layer. Many studies have identified the lattice fringe corresponding to χ-$Fe_5C_2(510)$ with a spacing of ∼2.05 Å,[18,60,62−64] suggesting the general presence of χ-Fe_5C_2 in FTS. Other lattice fringes, such as θ-$Fe_3C(111)$,[65,66] χ-$Fe_5C_2(202)$,[66] χ-$Fe_5C_2(\bar{2}02)$,[64] χ-$Fe_5C_2(\bar{3}11)$,[66] o-$Fe_7C_3(324)$,[66] and ε-$Fe_2C(101)$,[65] were detected occasionally, which have the interplanar spacing of 3.02, 2.19, 2.39, 2.65, 2.34, and 2.1 Å, respectively.

By using XPS and Raman spectroscopy, Yang *et al.* studied the surface of the as-synthesized χ-Fe_5C_2 nanoparticles,[60] which were prepared by using bromide as an inducing agent and $Fe(CO)_5$ as the precursor reagent. The XPS on the nanoparticle before FTS identified both the Fe_3O_4 phase and the carbide phase on the surface, as shown in Figure 2a: the surface has a C content of 70.55% and an O content of 18.27%. Consistently,

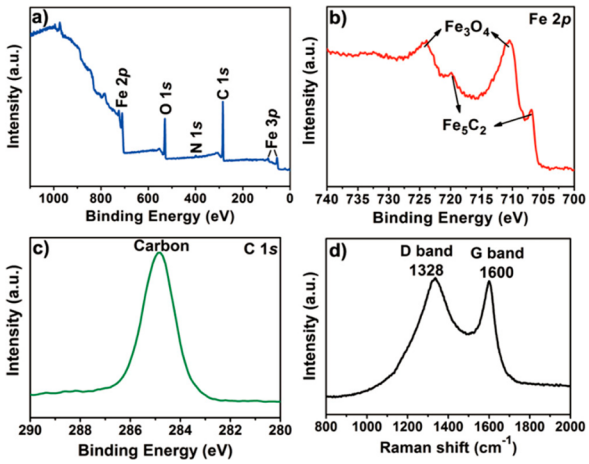

Figure 2. (a) XPS survey spectrum of χ-Fe_5C_2 nanoparticles. (b) Fe 2p XPS spectrum. (c) C 1s XPS spectrum. (d) Raman spectrum. Reproduced from ref60. Copyright 2012 American Chemical Society.

the Fe 2p XPS spectrum (Figure 2b) also has two peaks at ∼710 and ∼724 eV for Fe_3O_4 and two peaks at ∼707 and ∼720 eV for χ-Fe_5C_2. While their C 1s XPS spectrum (Figure 2c) with a single broad peak at ∼285 eV does not distinguish different C species, the Raman spectrum (Figure 2d) exhibits two bands, G-band at 1600 cm^{-1} and D band at 1328 cm^{-1}, respectively, assigned to the C=C stretching of polyaromatic rings and conjugated olefins, which suggests the existence of (amorphous) graphitic carbon. These graphitic carbon can be reacted off during FTS conditions, as shown by de Smit *et al.*, who studied the evolution of surface carbonaceous species at 1 MPa, 523 K.[17] The G and D bands of graphitic species increase significantly on the catalyst pretreated in low μ_C (heating to 623 K in 1% CO/H_2) but level off upon reaching 1 MPa on the catalyst pretreated in high μ_C (heating to 553 K in CO).

Furthermore, de Smit *et al.* investigated the evolution of C- and O-containing species on the surface of nanoparticle and bulk iron oxide using *in situ* XPS expriment under 0.3 Torr.[67] The samples were exposed to CO/H_2 (0.1 Torr CO/0.2 Torr H_2) and CO (0.3 Torr) at different temperatures after the reduction of H_2 (0.2 Torr). As shown in Figure 3a,b, they found that both nanoparticle and bulk samples show the increase of total coverage of C- and O-containing species at lower temperatures. When treated in CO/H_2, the nanoparticle mainly grows surface OH species (O 1s 530.8 eV) and carbonates (C 1s 289.8 eV and O 1s 531.9 eV), whereas the bulk sample exhibits a larger contribution of surface oxide (O 1s 530.1 eV) and carbides (C 1s 283.3 eV, $C_{carbide}/Fe = 0.07$ and 0.04 for bulk and nanoparticle, respectively). When treated in CO, the nanoparticle and bulk samples show a sharp increase of C/Fe ratio above 523 and 573 K, which is attributed to the buildup of Boudouard coke ($2CO \rightarrow CO_2 + C$, C 1s 284.6 eV). The nanoparticle sample has a larger content of bulk iron carbide (C 1s 283.3 eV, $C_{carbide}/Fe = 0.2$) and evolves an additional peak at 282.7 eV in the C 1s XPS spectra above 573 K, suggesting the presence of atomic carbon on the surface or in the subsurface. Their results indicate the atomic carbon can form more easily on the surface of nanoparticle iron oxide in reactive gas atmospheres. It should be mentioned that the C 1s XPS spectrum, however, cannot

https://doi.org/10.1021/acs.jpclett.2c00549
J. Phys. Chem. Lett. 2022, 13, 3342−3352

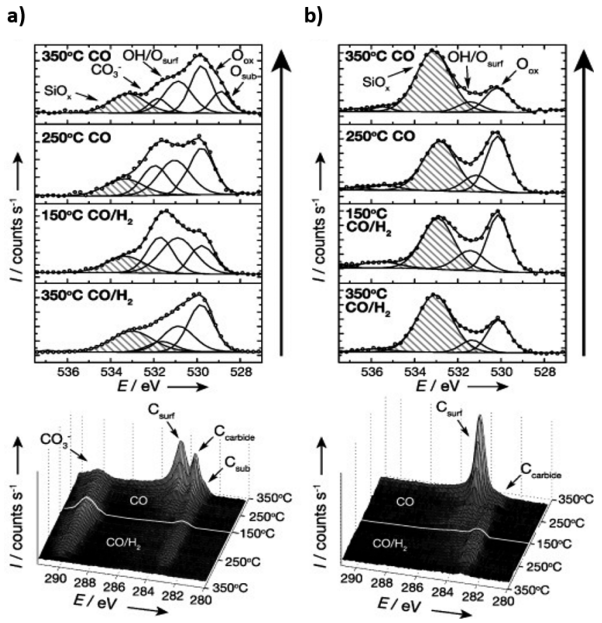

Figure 3. O 1s (top) and C 1s (bottom) XPS spectra of the (a) nanoparticle iron oxide and (b) bulk iron oxide during the treatment in 0.3 Torr CO/H_2 and 0.3 Torr CO at various temperatures. Hatched areas indicate the possible contribution of the SiO_x wafer. The spectra were acquired at 200 eV KE (ca. 7 Å inelastic mean free path, IMFP). Reproduced from ref 67. Copyright 2011 Wiley-VCH Verlag GmbH & Co. KGaA, Weinheim.

distinguish different "carbide" with the same coordination pattern, such as those in θ-Fe_3C, χ-Fe_5C_2, and Fe_7C_3.

Since 2000, a large number of theoretical studies have been performed on the surfaces of FeC_x. Although most of them utilized the bulk-truncated surfaces and did not consider the possible surface reconstruction induced by the coverage effect of surface species such as C, H, and CO, some interesting features of FeC_x surfaces have been gleaned. For example, Zhao *et al.* explored the bulk-truncated surfaces of Fe_4C, θ-Fe_3C, χ-Fe_5C_2, and ε-Fe_2C phases at different μ_C.[27,28] They found that $Fe_4C(100)$, θ-$Fe_3C(010)$, χ-$Fe_5C_2(100)$, and ε-$Fe_2C(1\bar{2}1)$ are the most stable surfaces in each FeC_x phase, which have the surface free energies of 1.18, 1.60, 1.70, and 1.80 J/m^2 at the low $\mu_C = -7.20$ eV, respectively. These stable surfaces share a very similar surface atom arrangement where each surface C atom coordinates with four surface Fe atoms and each Fe atom coordinates with two C atoms.

By using the SSW-NN method, our group investigated the likely surface reconstruction of FeC_x surfaces with different C coverages (variable Fe:C ratio on the surface).[51,61] We found that there are 13 surfaces with lower surface free energies, namely, θ-$Fe_3C(010)$, θ-$Fe_3C(031)$, θ-$Fe_3C(102)$, θ-$Fe_3C(131)$, χ-$Fe_5C_2(100)$, χ-$Fe_5C_2(510)$, χ-$Fe_5C_2(111)$, χ-$Fe_5C_2(021)$, o-Fe_7C_3-II(010), o-Fe_7C_3-II(071), η-$Fe_2C(011)$, η-$Fe_2C(110)$, and η-$Fe_2C(111)$. Their surface free energies are 1.50, 1.53, 1.65, 1.78, 1.68, 1.75, 1.81, 1.80, 1.88, 1.79, 1.72, 1.76, and 1.83 J/m^2 at $\mu_C = -6.90$ eV. The FeC_x surfaces are dynamic, involving not only structure reconstruction but also the change in composition, which leads to the surface Fe:C ratio being deviated from the bulk Fe:C ratio. Most of these stable surfaces have the same Fe:C ratio of Fe:C = 2 (Fe_2C) except χ-$Fe_5C_2(111)$ (Fe:C = 1.75) and η-$Fe_2C(110)$ (Fe:C = 1.50). These two surfaces with lower Fe:C ratio also have higher Fe−C coordination number, *i.e.*, 2.86 and 3 for χ-$Fe_5C_2(111)$ and η-$Fe_2C(110)$, respectively, compared to the other 11 surfaces, *i.e.*, θ-$Fe_3C(010)$, θ-$Fe_3C(031)$, θ-$Fe_3C(102)$, θ-$Fe_3C(131)$, χ-$Fe_5C_2(100)$, χ-$Fe_5C_2(510)$, χ-$Fe_5C_2(021)$, o-Fe_7C_3-II(010), o-Fe_7C_3-II(071), η-$Fe_2C(011)$, and η-$Fe_2C(111)$, which have the lower Fe−C coordination number of 2, 2.33, 2.67, 2.64, 2, 2.4, 2.7, 2, 2.5, 2.5, and 2.75, respectively. Obviously, most of these low-energy surfaces have the Fe−C coordination number within the range of 2.2−3, suggesting they are the potential active site for FTS according to the experiment by Wang *et al.*,[68] who found that the optimal Fe−C coordination number on the surface could be important for the catalytic performance. The catalyst with too high Fe−C coordination number (>3) produces more undesired CH_4, while that with too low Fe−C coordination number (<2.2) turns out to be inactive to FTS.

The adsorption of H and CO have also been examined on low-energy surfaces, which reveals that CO can adsorb generally on the exposed Fe sites of FeC_x surfaces. However, H adsorption differs from surface to surface: only eight surfaces, namely, θ-$Fe_3C(031)$, θ-$Fe_3C(102)$, θ-$Fe_3C(131)$, χ-$Fe_5C_2(510)$, χ-$Fe_5C_2(111)$, χ-$Fe_5C_2(021)$, o-Fe_7C_3-II(071), and η-$Fe_2C(111)$, that expose at least three adjacent 3-fold Fe_3 sites (except χ-$Fe_5C_2(111)$), as shown in Figure 4, can adsorb H atoms

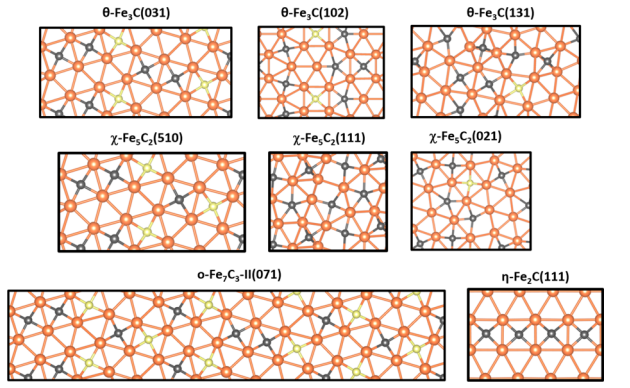

Figure 4. Top views on eight stable surfaces where the adsorption of H is exothermic. Seven surfaces have the Fe:C ratio of Fe:C = 2 (except χ-$Fe_5C_2(111)$; Fe:C = 1.75). Fe, orange; C, gray (upper) and yellow (lower).

exothermically ($G_{ad}(H) = -0.18$ eV for χ-$Fe_5C_2(111)$ and −0.40 to −0.30 eV for the other surfaces). They are thus the active site candidates for FTS. It should be noted that θ-$Fe_3C(031)$, χ-$Fe_5C_2(510)$, and o-Fe_7C_3-II(071) have a similar arrangement (Figure 4) in which the closely linked 3-fold Fe_3 sites are separated by four-coordinated planar C atoms in different ways.

FTS Activity on FeC_x. After one century of research, virtually every FeC_x detected in experiment has been suggested to be the active phase for FTS.[17,18,68,69] Nevertheless, χ-Fe_5C_2 is perhaps the most accepted active phase as it appears to be the major composition when the high product selectivity to long-chain hydrocarbons is reached in FTS. For example, de Smit *et al.* found that the catalyst with the higher content of χ-Fe_5C_2 before FTS (76 ± 5%) has a more stable and higher activity and selectivity to C_{4+} hydrocarbon chains with time-on-stream, while the catalyst with lower initial content of χ-Fe_5C_2 (χ-Fe_5C_2 + θ-Fe_3C, 51%) has a lower selectivity.[17] Even more precisely, Yang *et al.* showed that the as-synthesized single-phase χ-Fe_5C_2 nanoparticles achieved a 39% initial CO conversion rate and ~39% C_{5+} hydrocarbon selectivity at the conditions of 543 K

https://doi.org/10.1021/acs.jpclett.2c00549
J. Phys. Chem. Lett. 2022, 13, 3342−3352

and 3 MPa.[60] The single-phase χ-Fe_5C_2 catalyst can increase the initial CO conversion and C_{5+} product selectivity by 20% and 13% compared to the conventional catalyst reduced from Fe_2O_3.

One step further, Zhao *et al.* synthesized pure-phase Fe and various FeC_x (Fe_5C_2, Fe_7C_3, and Fe_2C) nanoparticles with similar particle size (~18 nm) and compared their FT activity at the conditions of 543 K and 3 MPa.[69] As shown in Figure 5a,

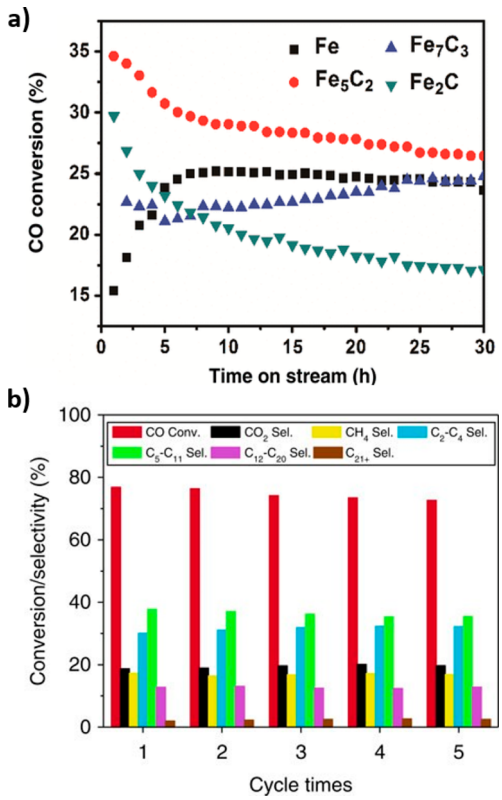

Figure 5. (a) CO conversion as a function of time over Fe, Fe_5C_2, Fe_7C_3, and Fe_2C catalysts (543 K, 3 MPa, $H_2/CO = 2/1$). Reproduced from ref 69. Copyright 2020 Zhao *et al.* (b) CO conversion and product distribution over RQ Fe catalyst in five successive cycles (443 K, 3 MPa at RT, $H_2/CO = 2/1$). The recovered catalyst is reused without reactivation. The hydrocarbon selectivities are normalized with the exception of CO_2. Reproduced from ref 57. Copyright 2014 Nature Publishing Group, a division of Macmillan Publishers Limited.

Fe_5C_2 and Fe_2C are the most active phases in terms of initial CO conversion. Fe_5C_2 can maintain the highest CO conversion rate in the whole time on stream, which decreases from 35% in the beginning to 27% approaching the steady state. While Fe_2C shows the second highest initial CO conversion rate (29.5%), it turns out to be the least active after 30 h (drops to 17%). Fe_7C_3 and Fe have the lowest initial CO conversion rate (22.5% and 15.2%, respectively), but both of them undergo the increase in CO conversion to ~25% after 30 h, apparently because of the phase transformation of these phases to the Fe_5C_2 phase. Finally (after 40 h), Fe and Fe_5C_2 exhibit the higher selectivity toward C_{5+} products (49% and 37%), while Fe_7C_3 and Fe_2C have undesirable selectivity of only 23% and 19% toward C_{5+} products.

ε-Fe_2C, the stable Fe carbide phase with the lowest Fe:C ratio, has raised much recent interest for its low-temperature (*e.g.*, 450 K) activity.[57,70] Considering that the formation of ε-Fe_2C is limited by C insertion kinetics, Xu *et al.* prepared ε-Fe_2C by the on-site carbidation of rapidly quenched skeletal iron (RQ Fe).[57] They found that the ε-Fe_2C-dominant RQ Fe catalyst exhibits superior initial activity for CO conversion to χ-Fe_5C_2-dominant RQ Fe catalyst by 75% at 443 K and high C_{5+} selectivity of 73% at 423 K. They also examined the stability of ε-Fe_2C-dominant RQ Fe catalyst at 443 K (Figure 5b). The CO conversion decreases by only 4.2%, and the product distributions hardly change from the first run to the fifth run in five successive cycles. This result agrees with the synchrotron XRD pattern of the catalyst after the stability test that ε-Fe_2C remains as the dominant phase. The high stability of the Fe_2C catalyst in RQ Fe compared to that prepared by Zhao *et al.*[69] may originate from the its smaller crystalline size (~8 nm), which can better resist the oxidative deactivation. Wang *et al.*[70] also found that ε-Fe_2C catalyst, synthesized via multistep gas pretreatment ($H_2/CO/N_2 = 2/1/10$, 443 K for 40 min) and carburization ($H_2/CO/N_2 = 3/2/2$, heat to 523 K at a rate of 0.5 K/min for 6 h), can achieve a low CO_2 selectivity (~5%) and high C_{5+} product selectivity (~50%) at a low CO conversion level (15%) at 508 K.

Aiming to shed light on the structure−activity relationship for Fe-based FTS, many theoretical studies have been conducted to understand the reaction mechanisms for CO activation and C−C coupling on the surfaces of FeC_x phases (mainly χ-Fe_5C_2). For example, our group studied the CO activation mechanism over the reconstructed χ-$Fe_5C_2(510)$,[51] the surface observed in the experiment,[60,64] and found that CO activation via direct dissociation can occur at the surface C vacancies (the barrier is 1.1 eV) that are created dynamically via hydrogenation to CH. The C−C coupling is an important step for producing long-chain products. Although CH_x coupling reaction, *e.g.*, using CH_2 as the monomer for chain propagation, has been verified on several transition metal surfaces,[71−73] it remains unclear whether the same mechanism is transferable to FeC_x surfaces. Until recently, a theoretical study by Yin *et al.*[74] compared the C_2 formation mechanisms on eight surfaces of χ-Fe_5C_2 and found that the CH_x coupling is more favorable than CO insertion pathway on all these surfaces, and the C + C coupling on χ-$Fe_5C_2(10\bar{1})$ is the fastest (the barrier is 1.26 eV) at low H coverage ($\theta_H/\theta_* \approx 10^{-4}$) according to their microkinetics result.

It should be kept in mind that FTS has many elementary steps, including CO activation, C−C couplings, and many hydrogenation reaction steps, including C hydrogenation and O removal. The active sites for different elementary steps may well not be the same, and thus it is important to identify the active sites for the reaction steps that are rate-determining and selectivity-controlling. From previous theoretical studies, the C hydrogenations have relative lower barriers (0.8−1.0 eV), and thus, they should not be the rate-determining step.[51,75] The O removal steps in H_2O and CO_2 formation appear to have a relative high barrier (1.0−1.5 eV),[76,77] and the kinetics of these steps have not been compared systematically with those for CO activation and C−C coupling.

Outlook. Through the collective efforts from both experiment and theory, tremedeous progress has been made in understanding Fe-based FTS. It is now established that several FeC_x phases, particularly Fe_5C_2 and Fe_2C, are most likely the active phases based on the thermodynamic stability data and the experimental activity analysis. Although multiple FeC_x phases coexist, the surfaces of different FeC_x phases can have identical chemical composition (*e.g.*, Fe:C = 2) and a great similarity in local structure. The catalytic role for other coexisting noncarbide phases, including FeO_x phases and amorphous and graphitic carbon, although not very clear, appears to be of minor significance. By reviewing the literature, we can outline some

https://doi.org/10.1021/acs.jpclett.2c00549
J. Phys. Chem. Lett. 2022, 13, 3342−3352

important open issues regarding FeC_x structures and the reaction mechanism as follows:

(i) The structure of the Fe_7C_3 bulk phase. Further evidence is required to characterize the *in situ* formed Fe_7C_3 bulk phase, in particular to distinguish the two o-phases, o-Fe_7C_3 and o-Fe_7C_3-II.

(ii) The junction structure between different FeC_x phases. Because multiple FeC_x phases coexist in FTS, the interfaces between them are of significance. If one phase can grow upon another phase readily, the concentration of bulk phase would become less relevant as to the surface active site.

(iii) The structure of FeC_x surfaces under the FTS condition. To date, most surface-sensitive characterization techniques cannot be operated under the FTS conditions, which limits the deep understanding of the *in situ* surface dynamics. Global neural network-based long-time atomic simulation could be utilized to trace the surface evolution kinetics.

(iv) The O cycle in FTS. After CO activiation, the O may end up in several places in FTS, including forming FeO_x phases, producing CO_2, H_2O, and even acohols. Many unknowns remain to be discovered regarding how the O cycle affects the FTS activity and selectivity.

Obviously, future investigations should be more directed toward real catalyst structures under FTS conditions, which calls for the development of new *in situ* techniques with high spatial and temporal resolution. On the other hand, theoretical studies, especially those based on machine learning techniques, should also play important roles for understanding the active site in Fe-based FTS.

To conclude this Perspective, we mention some emerging fields related to Fe-based catalysts that have generated much new interest in this "old" system:

(i) CO_2 hydrogenation to olefins or long-chain hydrocarbons that is of significance for carbon neutralization.[78−80] The oxide phases (mainly Fe_3O_4) were suggested to play an important role in the reaction, where a CO intermediate is generated from CO_2 via the reverse water gas shift reaction on Fe_3O_4.

(ii) The change of FTS selectivity. It is highly desirable to improve the FTS selectivity toward C_{5+} products or olefins over the selectivity to C_{1-4} products or paraffins. The catalyst modification by doping and restructuring is the focus of new experimental studies. For example, Fe_5C_2−Co heterostructured catalyst[81] and Fe−Zn−Na catalyst[79,82] were found to increase the selectivity to C_{5+} hydrocarbons and olefins. The oxygen-decorated Fe_5C_2 catalyst under photoirradiation condition[83] favors the selectivity to lower olefins (C_{2-4}). Apart from C_{5+} products and olefins, the oxygenate products are additional high-value chemicals being pursued in FTS technology. The Cu−Fe binary catalyst, for example, was shown to produce long-chain alcohols.[84−86] The catalyst combines the FeC_x ability toward C−C chain propagation and the Cu activity for CO insertion, the idea of which might be transferable for the design of other catalytic systems.

AUTHOR INFORMATION

Corresponding Authors

Cheng Shang − *Collaborative Innovation Center of Chemistry for Energy Material, Shanghai Key Laboratory of Molecular Catalysis and Innovative Materials, Key Laboratory of Computational Physical Science, Department of Chemistry, Fudan University, Shanghai 200433, China*; orcid.org/0000-0001-7486-1514; Email: cshang@fudan.edu.cn

Zhi-Pan Liu − *Collaborative Innovation Center of Chemistry for Energy Material, Shanghai Key Laboratory of Molecular Catalysis and Innovative Materials, Key Laboratory of Computational Physical Science, Department of Chemistry, Fudan University, Shanghai 200433, China; Key Laboratory of Synthetic and Self-Assembly Chemistry for Organic Functional Molecules, Shanghai Institute of Organic Chemistry, Chinese Academy of Sciences, Shanghai 200032, China*; orcid.org/0000-0002-2906-5217; Email: zpliu@fudan.edu.cn

Author

Qian-Yu Liu − *Collaborative Innovation Center of Chemistry for Energy Material, Shanghai Key Laboratory of Molecular Catalysis and Innovative Materials, Key Laboratory of Computational Physical Science, Department of Chemistry, Fudan University, Shanghai 200433, China*

Complete contact information is available at: https://pubs.acs.org/10.1021/acs.jpclett.2c00549

Notes

The authors declare no competing financial interest.

Biographies

Qianyu Liu received her B.S. from Fudan University in 2019. She is now a Ph.D. candidate in Department of Chemistry at Fudan University. Her current research interests are first-principles reaction dynamics of heterogeneous catalysis.

Cheng Shang received his B.S. and Ph.D. from Fudan University in 2008 and 2013, respectively. He was a postdoctoral associate at University of Cambridge (U.K.) from 2013 to 2015 and has been an associate professor in Department of Chemistry at Fudan University since 2015. His current research interests include (i) large-scale atomic simulation and software development and (ii) potential energy surface exploration.

Zhi-Pan Liu received his B.S. from Shanghai Jiaotong University in 1997 and his Ph.D from Queen's University of Belfast (U.K.) in 2003. He was a postdoctoral associate at University of Cambridge (U.K.) from 2003 to 2005 and has been a full professor in Department of Chemistry at Fudan University since 2005. His current research interests include (i) heterogeneous catalysis, (ii) global optimization and pathway search, and (iii) machine learning potential methods and simulation.

ACKNOWLEDGMENTS

This work was supported by the National Key Research and Development Program of China (2018YFA0208600), National Science Foundation of China (12188101, 22033003, 91945301, 91745201, 92145302, 22122301, and 92061112), and the Tencent Foundation for Xplorer Prize.

REFERENCES

(1) Fischer, F.; Tropsch, H. Uber die Herstellung Synthetischer Olgemische (Synthol) durch Aufbau aus Kohlenoxyd und Wasserstoff. *Brennst. Chem.* **1923**, *4*, 276−285.

(2) van de Loosdrecht, J.; Botes, F. G.; Ciobica, I. M.; Ferreira, A.; Gibson, P.; Moodley, D. J.; Saib, A. M.; Visagie, J. L.; Weststrate, C. J.; Niemantsverdriet, J. W. Fischer−Tropsch Synthesis: Catalysts and Chemistry. In *Comprehensive Inorganic Chemistry II*, 2nd ed.; Elsevier: Amsterdam, 2013; pp 525−557.

(3) de Smit, E.; Swart, I.; Creemer, J. F.; Hoveling, G. H.; Gilles, M. K.; Tyliszczak, T.; Kooyman, P. J.; Zandbergen, H. W.; Morin, C.; Weckhuysen, B. M.; de Groot, F. M. Nanoscale Chemical Imaging of a Working Catalyst by Scanning Transmission X-ray Microscopy. *Nature* **2008**, *456*, 222−225.
(4) Yu, G. B.; Sun, B.; Pei, Y.; Xie, S. H.; Yan, S. R.; Qiao, M. H.; Fan, K. N.; Zhang, X. X.; Zong, B. N. FexOy@C Spheres as an Excellent Catalyst for Fischer−Tropsch Synthesis. *J. Am. Chem. Soc.* **2010**, *132*, 935−937.
(5) Torres Galvis, H. M. T.; Bitter, J. H.; Davidian, T.; Ruitenbeek, M.; Dugulan, A. I.; de Jong, K. P. Iron Particle Size Effects for Direct Production of Lower Olefins from Synthesis Gas. *J. Am. Chem. Soc.* **2012**, *134*, 16207−16215.
(6) Torres Galvis, H. M. T.; Bitter, J. H.; Khare, C. B.; Ruitenbeek, M.; Dugulan, A. I.; de Jong, K. P. Supported Iron Nanoparticles as Catalysts for Sustainable Production of Lower Olefins. *Science* **2012**, *335*, 835−838.
(7) Santos, V. P.; Wezendonk, T. A.; Jaen, J. J. D.; Dugulan, A. I.; Nasalevich, M. A.; Islam, H. U.; Chojecki, A.; Sartipi, S.; Sun, X.; Hakeem, A. A.; Koeken, A. C. J.; Ruitenbeek, M.; Davidian, T.; Meima, G. R.; Sankar, G.; Kapteijn, F.; Makkee, M.; Gascon, J. Metal Organic Framework-Mediated Synthesis of Highly Active and Stable Fischer−Tropsch Catalysts. *Nat. Commun.* **2015**, *6*, 6451.
(8) Xu, Y. F.; Li, X. Y.; Gao, J. H.; Wang, J.; Ma, G. Y.; Wen, X. D.; Yang, Y.; Li, Y. W.; Ding, M. Y. A Hydrophobic FeMn@Si Catalyst Increases Olefins from Syngas by Suppressing C1 By-Products. *Science* **2021**, *371*, 610−613.
(9) Hägg, G. Pulverphotogramme eines Neuen Eisencarbides. *Z. Kristallogr. Cryst. Mater.* **1934**, *89*, 92−94.
(10) Eckstrom, H. C.; Adcock, W. A. A New Iron Carbide in Hydrocarbon Synthesis Catalysts. *J. Am. Chem. Soc.* **1950**, *72*, 1042−1043.
(11) Hofer, L. J. E.; Cohn, E. M.; Peebles, W. C. The Modifications of the Carbide, Fe2C - Their Properties and Identification. *J. Am. Chem. Soc.* **1949**, *71*, 189−195.
(12) Anderson, R. B.; Hofer, L. J. E.; Cohn, E. M.; Seligman, B. Studies of the Fischer−Tropsch Synthesis. IX. Phase Changes of Iron Catalysts in the Synthesis. *J. Am. Chem. Soc.* **1951**, *73*, 944−946.
(13) de Smit, E.; Weckhuysen, B. M. The Renaissance of Iron-Based Fischer−Tropsch Synthesis: on the Multifaceted Catalyst Deactivation Behaviour. *Chem. Soc. Rev.* **2008**, *37*, 2758−2781.
(14) Fasiska, E.; Jeffrey, G. On the Cementite Structure. *Acta Crystallogr.* **1965**, *19*, 463−471.
(15) Duggin, M. J.; Hofer, L. J. E. Nature of χ-Iron Carbide. *Nature* **1966**, *212*, 248.
(16) Herbstein, F. H.; Snyman, J. A. Identification of Eckstrom-Adcock Iron Carbide as Fe7C3. *Inorg. Chem.* **1964**, *3*, 894−896.
(17) de Smit, E.; Cinquini, F.; Beale, A. M.; Safonova, O. V.; van Beek, W.; Sautet, P.; Weckhuysen, B. M. Stability and Reactivity of ϵ-χ-θ Iron Carbide Catalyst Phases in Fischer−Tropsch Synthesis: Controlling μc. *J. Am. Chem. Soc.* **2010**, *132*, 14928−14941.
(18) Chang, Q.; Zhang, C.; Liu, C.; Wei, Y.; Cheruvathur, A. V.; Dugulan, A. I.; Niemantsverdriet, J. W.; Liu, X.; He, Y.; Qing, M.; Zheng, L.; Yun, Y.; Yang, Y.; Li, Y. Relationship between Iron Carbide Phases (ϵ-Fe2C, Fe7C3, and χ-Fe5C2) and Catalytic Performances of Fe/SiO2 Fischer−Tropsch Catalysts. *ACS Catal.* **2018**, *8*, 3304−3316.
(19) Dwyer, D. J.; Somorjai, G. A. Hydrogenation of CO and CO2 over Iron Foils - Correlations of Rate, Product Distribution, and Surface Composition. *J. Catal.* **1978**, *52*, 291−301.
(20) Dwyer, D. J.; Somorjai, G. A. The Role of Readsorption in Determining the Product Distribution during CO Hydrogenation over Fe Single Crystals. *J. Catal.* **1979**, *56*, 249−257.
(21) Krebs, H. J.; Bonzel, H. P.; Gafner, G. Model Study of the Hydrogenation of CO over Polycrystalline Iron. *Surf. Sci.* **1979**, *88*, 269−283.
(22) Lee, Y. C.; Tong, P.; Montano, P. A. Deposition of Iron on MgO(100): Reaction of CO and H2. *Surf. Sci.* **1987**, *181*, 559−572.
(23) Eliason, S. A.; Bartholomew, C. H. Temperature-Programmed Reaction Study of Carbon Transformations on Iron Fischer−Tropsch Catalysts during Steady-State Synthesis. *Stud. Surf. Sci. Catal.* **1997**, *111*, 517−526.
(24) Xu, J.; Bartholomew, C. R. Temperature-Programmed Hydrogenation (TPH) and in situ Mössbauer Spectroscopy Studies of Carbonaceous Species on Silica-Supported Iron Fischer−Tropsch Catalysts. *J. Phys. Chem. B* **2005**, *109*, 2392−2403.
(25) Mannie, G. J. A.; Lammich, L.; Li, Y.-W.; Niemantsverdriet, J. W.; Lauritsen, J. V. Monolayer Iron Carbide Films on Au(111) as a Fischer−Tropsch Model Catalyst. *ACS Catal.* **2014**, *4*, 3255−3260.
(26) Li, Y. J.; Li, Z. S.; Ahsen, A.; Lammich, L.; Mannie, G. J. A.; Niemantsverdriet, J. W. H.; Lauritsen, J. V. Atomically Defined Iron Carbide Surface for Fischer−Tropsch Synthesis Catalysis. *ACS Catal.* **2019**, *9*, 1264−1273.
(27) Zhao, S.; Liu, X.-W.; Huo, C.-F.; Li, Y.-W.; Wang, J.; Jiao, H. Surface Morphology of Hägg Iron Carbide (χ-Fe5C2) from ab initio Atomistic Thermodynamics. *J. Catal.* **2012**, *294*, 47−53.
(28) Zhao, S.; Liu, X.-W.; Huo, C.-F.; Li, Y.-W.; Wang, J.; Jiao, H. Determining Surface Structure and Stability of ϵ-Fe2C, χ-Fe5C2, θ-Fe3C and Fe4C Phases under Carburization Environment from Combined DFT and Atomistic Thermodynamic Studies. *Catalysis, Structure & Reactivity* **2015**, *1*, 44−60.
(29) Pham, T. H.; Duan, X.; Qian, G.; Zhou, X.; Chen, D. CO Activation Pathways of Fischer−Tropsch Synthesis on χ-Fe5C2 (510): Direct versus Hydrogen-Assisted CO Dissociation. *J. Phys. Chem. C* **2014**, *118*, 10170−10176.
(30) Broos, R. J. P.; Zijlstra, B.; Filot, I. A. W.; Hensen, E. J. M. Quantum-Chemical DFT Study of Direct and H- and C-Assisted CO Dissociation on the χ-Fe5C2 Hagg Carbide. *J. Phys. Chem. C* **2018**, *122*, 9929−9938.
(31) Broos, R. J. P.; Klumpers, B.; Zijlstra, B.; Filot, I. A. W.; Hensen, E. J. M. A Quantum-Chemical Study of the CO Dissociation Mechanism on Low-Index Miller Planes of θ-Fe3C. *Catal. Today* **2020**, *342*, 152−160.
(32) Chun, H. J.; Kim, Y. T. Theoretical Study of CO Adsorption and Activation on Orthorhombic Fe7C3(001) Surfaces for Fischer−Tropsch Synthesis Using Density Functional Theory Calculations. *Energies* **2021**, *14*, 563.
(33) Ozbek, M. O.; Niemantsverdriet, J. W. Elementary Reactions of CO and H2 on C-terminated χ-Fe5C2(001) Surfaces. *J. Catal.* **2014**, *317*, 158−166.
(34) Huo, C. F.; Li, Y. W.; Wang, J. G.; Jiao, H. J. Insight into CH4 Formation in Iron-Catalyzed Fischer−Tropsch Synthesis. *J. Am. Chem. Soc.* **2009**, *131*, 14713−14721.
(35) Chen, B.; Wang, D.; Duan, X.; Liu, W.; Li, Y.; Qian, G.; Yuan, W.; Holmen, A.; Zhou, X.; Chen, D. Charge-Tuned CO Activation over a χ-Fe5C2 Fischer−Tropsch Catalyst. *ACS Catal.* **2018**, *8*, 2709−2714.
(36) He, Y.; Zhao, P.; Meng, Y.; Guo, W.; Yang, Y.; Li, Y.-W.; Huo, C.-F.; Wen, X.-D. Hunting the Correlation between Fe5C2 Surfaces and Their Activities on CO: The Descriptor of Bond Valence. *J. Phys. Chem. C* **2018**, *122*, 2806−2814.
(37) Cheng, J.; Hu, P.; Ellis, P.; French, S.; Kelly, G.; Lok, C. M. Density Functional Theory Study of Iron and Cobalt Carbides for Fischer−Tropsch Synthesis. *J. Phys. Chem. C* **2010**, *114*, 1085−1093.
(38) Curulla-Ferre, D.; Govender, A.; Bromfield, T. C.; Niemantsverdriet, J. W. A DFT Study of the Adsorption and Dissociation of CO on Sulfur-Precovered Fe(100). *J. Phys. Chem. B* **2006**, *110*, 13897−13904.
(39) Huo, C. F.; Ren, J.; Li, Y. W.; Wang, J. G.; Jiao, H. J. CO Dissociation on Clean and Hydrogen Precovered Fe(111) Surfaces. *J. Catal.* **2007**, *249*, 174−184.
(40) Ojeda, M.; Nabar, R.; Nilekar, A. U.; Ishikawa, A.; Mavrikakis, M.; Iglesia, E. CO Activation Pathways and the Mechanism of Fischer−Tropsch Synthesis. *J. Catal.* **2010**, *272*, 287−297.
(41) He, Y.; Zhao, P.; Yin, J.; Guo, W.; Yang, Y.; Li, Y.-W.; Huo, C.-F.; Wen, X.-D. CO Direct versus H-Assisted Dissociation on Hydrogen Coadsorbed χ-Fe5C2 Fischer−Tropsch Catalysts. *J. Phys. Chem. C* **2018**, *122*, 20907−20917.

https://doi.org/10.1021/acs.jpclett.2c00549
J. Phys. Chem. Lett. 2022, 13, 3342−3352

(42) Gracia, J. M.; Prinsloo, F. F.; Niemantsverdriet, J. W. Mars-van Krevelen-like Mechanism of CO Hydrogenation on an Iron Carbide Surface. *Catal. Lett.* **2009**, *133*, 257−261.
(43) Li, S.; Yang, J.; Song, C.; Zhu, Q.; Xiao, D.; Ma, D. Iron Carbides: Control Synthesis and Catalytic Applications in COx Hydrogenation and Electrochemical HER. *Adv. Mater.* **2019**, *31*, 1901796.
(44) Zhai, P.; Li, Y.; Wang, M.; Liu, J.; Cao, Z.; Zhang, J.; Xu, Y.; Liu, X.; Li, Y.-W.; Zhu, Q.; Xiao, D.; Wen, X.-D.; Ma, D. Development of Direct Conversion of Syngas to Unsaturated Hydrocarbons Based on Fischer−Tropsch Route. *Chem.* **2021**, *7*, 3027−3051.
(45) Torres Galvis, H. M.; de Jong, K. P. Catalysts for Production of Lower Olefins from Synthesis Gas: A Review. *ACS Catal.* **2013**, *3*, 2130−2149.
(46) Shang, C.; Zhang, X. J.; Liu, Z. P. Stochastic Surface Walking Method for Crystal Structure and Phase Transition Pathway Prediction. *Phys. Chem. Chem. Phys.* **2014**, *16*, 17845−17856.
(47) Huang, S. D.; Shang, C.; Zhang, X. J.; Liu, Z. P. Material Discovery by Combining Stochastic Surface Walking Global Optimization with a Neural Network. *Chem. Sci.* **2017**, *8*, 6327−6337.
(48) Huang, S. D.; Shang, C.; Kang, P. L.; Liu, Z. P. Atomic Structure of Boron Resolved Using Machine Learning and Global Sampling. *Chem. Sci.* **2018**, *9*, 8644.
(49) Huang, S. D.; Shang, C.; Kang, P. L.; Zhang, X. J.; Liu, Z. P. LASP: Fast Global Potential Energy Surface Exploration. *WIREs Comput Mol Sci* **2019**, *9*, No. e1415.
(50) Shang, C.; Liu, Z. P. Stochastic Surface Walking Method for Structure Prediction and Pathway Searching. *J. Chem. Theory Comput.* **2013**, *9*, 1838−1845.
(51) Liu, Q.-Y.; Shang, C.; Liu, Z.-P. In Situ Active Site for CO Activation in Fe-Catalyzed Fischer−Tropsch Synthesis from Machine Learning. *J. Am. Chem. Soc.* **2021**, *143*, 11109−11120.
(52) Le Caer, G.; Dubois, J. M.; Senateur, J. P. Etude par Spectrométrie Mössbauer des Carbures de Fer Fe3C et Fe5C2. *J. Solid State Chem.* **1976**, *19*, 19−28.
(53) Liu, X. W.; Zhao, S.; Meng, Y.; Peng, Q.; Dearden, A. K.; Huo, C. F.; Yang, Y.; Li, Y. W.; Wen, X. D. Mossbauer Spectroscopy of Iron Carbides: From Prediction to Experimental Confirmation. *Sci. Rep.* **2016**, *6*, 26184.
(54) Niemantsverdriet, J. W.; Vanderkraan, A. M.; Vandijk, W. L.; Vanderbaan, H. S. Behavior of Metallic Iron Catalysts during Fischer−Tropsch Synthesis Studied with Mössbauer-Spectroscopy, X-Ray-Diffraction, Carbon Content Determination, and Reaction Kinetic Measurements. *J. Phys. Chem.* **1980**, *84*, 3363−3370.
(55) Liu, X.-W.; Cao, Z.; Zhao, S.; Gao, R.; Meng, Y.; Zhu, J.-X.; Rogers, C.; Huo, C.-F.; Yang, Y.; Li, Y.-W.; Wen, X.-D. Iron Carbides in Fischer−Tropsch Synthesis: Theoretical and Experimental Understanding in Epsilon-Iron Carbide Phase Assignment. *J. Phys. Chem. C* **2017**, *121*, 21390−21396.
(56) Lecaer, G.; Simon, A.; Lorenzo, A.; Genin, J. M. Mössbauer Effect Study of ε-Carbide - Influence of Particle Size. *Phys. Status Solidi A* **1971**, *6*, K97−K100.
(57) Xu, K.; Sun, B.; Lin, J.; Wen, W.; Pei, Y.; Yan, S.; Qiao, M.; Zhang, X.; Zong, B. ε-Iron Carbide as a Low-Temperature Fischer−Tropsch Synthesis Catalyst. *Nat. Commun.* **2014**, *5*, 5783.
(58) Williamson, D. L.; Nakazawa, K.; Krauss, G. A Study of the Early Stages of Tempering in an Fe-1.2 Pct Alloy. *Metall. Trans. A* **1979**, *10*, 1351−1363.
(59) Zhang, X. J.; Shang, C.; Liu, Z. P. Pressure-Induced Silica Quartz Amorphization Studied by Iterative Stochastic Surface Walking Reaction Sampling. *Phys. Chem. Chem. Phys.* **2017**, *19*, 4725−4733.
(60) Yang, C.; Zhao, H.; Hou, Y.; Ma, D. Fe5C2 Nanoparticles: A Facile Bromide-Induced Synthesis and as an Active Phase for Fischer−Tropsch Synthesis. *J. Am. Chem. Soc.* **2012**, *134*, 15814−15821.
(61) Liu, Q. Y.; Liu, Z. P. RDF Simulation, θ-Fe3C(031), θ-Fe3C(102), θ-Fe3C(131), χ-Fe5C2(021), o-Fe7C3-II(071) energetics. Data from our own unpublished computational data.
(62) Park, J. C.; Yeo, S. C.; Chun, D. H.; Lim, J. T.; Yang, J. I.; Lee, H. T.; Hong, S.; Lee, H. M.; Kim, C. S.; Jung, H. Highly Activated K-Doped Iron Carbide Nanocatalysts Designed by Computational Simulation for Fischer−Tropsch Synthesis. *J. Mater. Chem. A* **2014**, *2*, 14371−14379.
(63) Li, Y.; Li, R. Z.; Li, Z. H.; Wei, W. Q.; Ouyang, S. X.; Yuan, H.; Zhang, T. R. Effect of Support on Catalytic Performance of Photothermal Fischer−Tropsch Synthesis to Produce Lower Olefins over Fe5C2-based Catalysts. *Chem. Res. Chin. Univ.* **2020**, *36*, 1006−1012.
(64) Jiang, F.; Liu, B.; Li, W.; Zhang, M.; Li, Z.; Liu, X. Two-Dimensional Graphene-Directed Formation of Cylindrical Iron Carbide Nanocapsules for Fischer−Tropsch Synthesis. *Catal. Sci. Technol.* **2017**, *7*, 4609−4621.
(65) Lyu, S.; Wang, L.; Li, Z.; Yin, S. K.; Chen, J.; Zhang, Y. H.; Li, J. L.; Wang, Y. Stabilization of ε-Iron Carbide as High-Temperature Catalyst under Realistic Fischer−Tropsch Synthesis Conditions. *Nat. Commun.* **2020**, *11*, 6219.
(66) Zhuo, O.; Yang, L. J.; Gao, F. J.; Xu, B. L.; Wu, Q.; Fan, Y. N.; Zhang, Y.; Jiang, Y. F.; Huang, R. S.; Wang, X. Z.; Hu, Z. Stabilizing the Active Phase of Iron-Based Fischer−Tropsch Catalysts for Lower Olefins: Mechanism and Strategy. *Chem. Sci.* **2019**, *10*, 6083−6090.
(67) de Smit, E.; van Schooneveld, M. M.; Cinquini, F.; Bluhm, H.; Sautet, P.; de Groot, F. M.; Weckhuysen, B. M. On the Surface Chemistry of Iron Oxides in Reactive Gas Atmospheres. *Angew. Chem., Int. Ed.* **2011**, *50*, 1584−1588.
(68) Wang, J.; Huang, S.; Howard, S.; Muir, B. W.; Wang, H.; Kennedy, D. F.; Ma, X. Elucidating Surface and Bulk Phase Transformation in Fischer−Tropsch Synthesis Catalysts and Their Influences on Catalytic Performance. *ACS Catal.* **2019**, *9*, 7976−7983.
(69) Zhao, H.; Liu, J.-X.; Yang, C.; Yao, S.; Su, H.-Y.; Gao, Z.; Dong, M.; Wang, J.; Hou, Y.; Li, W.-X.; Ma, D. Synthesis of Iron-Carbide Nanoparticles: Identification of the Active Phase and Mechanism of Fe-Based Fischer−Tropsch Synthesis. *CCS Chem.* **2021**, *3*, 2712−2724.
(70) Wang, P.; Chen, W.; Chiang, F. K.; Dugulan, A. I.; Song, Y. J.; Pestman, R.; Zhang, K.; Yao, J. S.; Feng, B.; Miao, P.; Xu, W. N.; Hensen, E. J. M. Synthesis of Stable and Low-CO2 Selective ε-Iron Carbide Fischer−Tropsch Catalysts. *Sci. Adv.* **2018**, *4*, No. eaau2947.
(71) Brady, R. C.; Pettit, R. Reactions of Diazomethane on Transition-Metal Surfaces and Their Relationship to the Mechanism of the Fischer−Tropsch Reaction. *J. Am. Chem. Soc.* **1980**, *102*, 6181−6182.
(72) Brady, R. C.; Pettit, R. On the Mechanism of the Fischer−Tropsch Reaction - the Chain Propagation Step. *J. Am. Chem. Soc.* **1981**, *103*, 1287−1289.
(73) Turner, M. L.; Marsih, N.; Mann, B. E.; Quyoum, R.; Long, H. C.; Maitlis, P. M. Investigations by C-13 NMR Spectroscopy of Ethene-Initiated Catalytic CO Hydrogenation. *J. Am. Chem. Soc.* **2002**, *124*, 10456−10472.
(74) Yin, J.; Liu, X.; Liu, X.-W.; Wang, H.; Wan, H.; Wang, S.; Zhang, W.; Zhou, X.; Teng, B.-T.; Yang, Y.; Li, Y.-W.; Cao, Z.; Wen, X.-D. Theoretical Exploration of Intrinsic Facet-Dependent CH4 and C2 Formation on Fe5C2 Particle. *Appl. Catal., B* **2020**, *278*, 119308.
(75) Zhang, M.; Ren, J.; Yu, Y. Insights into the Hydrogen Coverage Effect and the Mechanism of Fischer−Tropsch to Olefins Process on Fe5C2 (510). *ACS Catal.* **2020**, *10*, 689−701.
(76) Ozbek, M. O.; Niemantsverdriet, J. W. Methane, Formaldehyde and Methanol Formation Pathways from Carbon Monoxide and Hydrogen on the (001) Surface of the Iron Carbide χ-Fe5C2. *J. Catal.* **2015**, *325*, 9−18.
(77) Liu, B.; Li, W.; Zheng, J.; Lin, Q.; Zhang, X.; Zhang, J.; Jiang, F.; Xu, Y.; Liu, X. CO2 Formation Mechanism in Fischer−Tropsch Synthesis over Iron-Based Catalysts: A Combined Experimental and Theoretical Study. *Catal. Sci. Technol.* **2018**, *8*, 5288−5301.
(78) Xu, Y.; Zhai, P.; Deng, Y. C.; Xie, J. L.; Liu, X.; Wang, S.; Ma, D. Highly Selective Olefin Production from CO2 Hydrogenation on Iron Catalysts: A Subtle Synergy between Manganese and Sodium Additives. *Angew. Chem., Int. Ed.* **2020**, *59*, 21736−21744.
(79) Zhang, Z. Q.; Yin, H. R.; Yu, G. D.; He, S.; Kang, J. C.; Liu, Z. M.; Cheng, K.; Zhang, Q. H.; Wang, Y. Selective Hydrogenation of CO2 and CO into Olefins over Sodium- and Zinc-Promoted Iron Carbide Catalysts. *J. Catal.* **2021**, *395*, 350−361.

https://doi.org/10.1021/acs.jpclett.2c00549
J. Phys. Chem. Lett. 2022, 13, 3342−3352

(80) Han, Y.; Fang, C. Y.; Ji, X. W.; Wei, J.; Ge, Q. J.; Sun, J. Interfacing with Carbonaceous Potassium Promoters Boosts Catalytic CO2 Hydrogenation of Iron. *ACS Catal.* **2020**, *10*, 12098−12108.
(81) Yang, C.; Zhao, B.; Gao, R.; Yao, S.; Zhai, P.; Li, S.; Yu, J.; Hou, Y.; Ma, D. Construction of Synergistic Fe5C2/Co Heterostructured Nanoparticles as an Enhanced Low Temperature Fischer−Tropsch Synthesis Catalyst. *ACS Catal.* **2017**, *7*, 5661−5667.
(82) Zhai, P.; Xu, C.; Gao, R.; Liu, X.; Li, M.; Li, W.; Fu, X.; Jia, C.; Xie, J.; Zhao, M.; Wang, X.; Li, Y.-W.; Zhang, Q.; Wen, X.-D.; Ma, D. Highly Tunable Selectivity for Syngas-Derived Alkenes over Zinc and Sodium-Modulated Fe5C2 Catalyst. *Angew. Chem., Int. Ed.* **2016**, *55*, 9902−9907.
(83) Gao, W.; Gao, R.; Zhao, Y.; Peng, M.; Song, C.; Li, M.; Li, S.; Liu, J.; Li, W.; Deng, Y.; Zhang, M.; Xie, J.; Hu, G.; Zhang, Z.; Long, R.; Wen, X.-D.; Ma, D. Photo-Driven Syngas Conversion to Lower Olefins over Oxygen-Decorated Fe5C2 Catalyst. *Chem.* **2018**, *4*, 2917−2928.
(84) Li, Y. W.; Gao, W.; Peng, M.; Zhang, J. B.; Sun, J.; Xu, Y.; Hong, S.; Liu, X.; Liu, X. W.; Wei, M.; Zhang, B. S.; Ma, D. Interfacial Fe5C2-Cu Catalysts toward Low-Pressure Syngas Conversion to Long-Chain Alcohols. *Nat. Commun.* **2020**, *11*, 61.
(85) Lu, Y.; Zhang, R. G.; Cao, B. B.; Ge, B. H.; Tao, F. F.; Shan, J. J.; Nguyen, L.; Bao, Z. H.; Wu, T. P.; Pote, J. W.; Wang, B. J.; Yu, F. Elucidating the Copper-Hägg Iron Carbide Synergistic Interactions for Selective CO Hydrogenation to Higher Alcohols. *ACS Catal.* **2017**, *7*, 5500−5512.
(86) Luk, H. T.; Mondelli, C.; Mitchell, S.; Siol, S.; Stewart, J. A.; Ferre, D. C.; Perez-Ramirez, J. Role of Carbonaceous Supports and Potassium Promoter on Higher Alcohols Synthesis over Copper-Iron Catalysts. *ACS Catal.* **2018**, *8*, 9604−9618.

https://doi.org/10.1021/acs.jpclett.2c00549
J. Phys. Chem. Lett. 2022, 13, 3342−3352